Journal of Biomedical Optics

BiomedicalOptics.SPIEDigitalLibrary.org

Quantum cascade laser–based hyperspectral imaging of biological tissue

Niels Kröger
Alexander Egl
Maria Engel
Norbert Gretz
Katharina Haase
Iris Herpich
Bettina Kränzlin
Sabine Neudecker
Annemarie Pucci
Arthur Schönhals
Jochen Vogt
Wolfgang Petrich

SPIE.

Journal of Biomedical Optics 19(11), 111607 (November 2014)

Quantum cascade laser–based hyperspectral imaging of biological tissue

Niels Kröger,[a,*] Alexander Egl,[a] Maria Engel,[a] Norbert Gretz,[b] Katharina Haase,[a] Iris Herpich,[a] Bettina Kränzlin,[b] Sabine Neudecker,[b] Annemarie Pucci,[a] Arthur Schönhals,[a] Jochen Vogt,[a] and Wolfgang Petrich[a]
[a]University of Heidelberg, Kirchhoff Institute for Physics, Im Neuenheimer Feld 227, Heidelberg, 69120 Germany
[b]University of Heidelberg, Medical Faculty Mannheim, Medical Research Center, Theodor-Kutzer-Ufer 1-3, Mannheim, 68167 Germany

Abstract. The spectroscopy of analyte-specific molecular vibrations in tissue thin sections has opened up a path toward histopathology without the need for tissue staining. However, biomedical vibrational imaging has not yet advanced from academic research to routine histopathology due to long acquisition times for the microscopic hyperspectral images and/or cost and availability of the necessary equipment. Here we show that the combination of a fast-tuning quantum cascade laser with a microbolometer array detector allows for a rapid image acquisition and bares the potential for substantial cost reduction. A 3.1×2.8 mm^2 unstained thin section of mouse jejunum has been imaged in the 9.2 to 9.7 μm wavelength range (spectral resolution $\sim$1 cm^{-1}) within 5 min with diffraction limited spatial resolution. The comparison of this hyperspectral imaging approach with standard Fourier transform infrared imaging or mapping of the identical sample shows a reduction in acquisition time per wavenumber interval and image area by more than one or three orders of magnitude, respectively. [DOI: 10.1117/1.JBO.19.11.111607]

Keywords: quantum cascade laser; hyperspectral imaging; chemical imaging; infrared microscopy; Fourier transform infrared spectroscopy; microbolometer array; biomedical vibrational spectroscopy; focal plane array.

Paper 140100SSPR received Feb. 20, 2014; revised manuscript received May 12, 2014; accepted for publication May 16, 2014; published online Jun. 26, 2014.

1 Introduction

The combination of microscopy and infrared spectroscopy has rapidly progressed over the past two decades and it has become a sensitive method for the chemical imaging of unstained biological tissue sections.[1,2] Microscopy images are acquired at different wavelengths of infrared radiation, and the spectra are typically evaluated by means of multivariate data analysis.[3] Among these methods is the cluster analysis, which allows for the investigation of morphology[4] and chemical composition. Information obtained by cluster analysis can be used, for example, to discriminate between healthy tissue and tumors.[5] Prior studies have demonstrated that some heterogeneities in tumor tissue that remain undetectable when using conventional histological staining become visible after analyzing the hyperspectral data collected in the mid-infrared region.[6] Indeed, there have been instances in which tissue deemed normal by traditional histological methods was identified as abnormal by using hyperspectral data.[7–9]

The standard approach for obtaining hyperspectral data in the mid-infrared region is Fourier transform infrared mapping (FT-IR mapping). In these measurements, data are acquired point by point, which, thus, allows for a complete mapping of the sample. One major drawback of this technique is the long acquisition time that is necessary for creating hyperspectral images of samples in the millimeter size range. Depending on the desired resolution and sample size, data acquisition can take up to several days, which limits the practical use of the technique.

*Address all correspondence to: Niels Kröger, E-mail: niels.kroeger@kip.uni-heidelberg.de

This drawback of long acquisition times can be mitigated by using a synchrotron as an infrared radiation source. Especially when the highest spatial resolution is required, the high brilliance of the synchrotron is highly beneficial since it provides high flux at small apertures.[10,11]

A second approach is to use a focal plane array (FPA) detector instead of a single-element detector, which allows for the parallelization of the point-like acquisition of FT-IR spectra. This method is called FT-IR imaging. The usual approach is to illuminate the field of view of the detector with a thermal source for FT-IR imaging. The subsequent use of FT-IR mapping on areas of interest in the image with a synchrotron radiation source can provide additional information.[12] Recently great effort has been put into enlarging the illuminated sample area in synchrotron-based FT-IR imaging to further increase spatial resolution and reduce acquisition time.[13–15]

However, synchrotron radiation is unavailable for most laboratories and FPAs suitable for FT-IR spectroscopy are very costly, leaving slow FT-IR mapping with a thermal radiation source the only option for many experiments.

The development of quantum cascade lasers (QCL) provides an alternative for speeding up hyperspectral imaging.[16] Commercially available external cavity quantum cascade lasers (EC-QCL) combine high brilliance with tuning ranges of up to several hundred wavenumbers and high spectral energy density.[17]

Parallel to the developments in QCL technology, rapid developments in microbolometer FPA technology has taken place.[18] These detectors are cheap when compared to mercury-cadmium-telluride (MCT)-based FPAs. So far, low frame rates and relatively low signal-to-noise ratios have prevented microbolometer FPA from reaching wide-spread use in FT-IR imaging.

In this paper, we discuss the combined impact of the high spectral power density of a QCL with the advantages of a microbolometer array. Hyperspectral images can be obtained by synchronizing the detuning of a tunable QCL with a microbolometer FPA, rendering low frame rates irrelevant.[19,20] This new approach allows for highly parallelized data acquisition. However, signal-to-noise levels are still inferior to those of FT-IR spectroscopy. The high-speed detection and identification of explosive particles using QCL-based microspectroscopy in combination with a microbolometer FPA has been demonstrated.[21] However, it remains unclear if image quality and signal-to-noise ratios are sufficient for usage of such a device in forms of biomedical vibrational spectroscopy, such as histopathology.

In this study, we use a custom-built setup to perform hyperspectral imaging on an unstained slice of mouse jejunum, combining an EC-QCL and a microbolometer FPA. For comparison, the same sample is also investigated using a standard, commercial FT-IR mapping and FT-IR imaging setup.

2 Materials and Methods

2.1 *Sample Preparation*

A sample of jejunum from a male Naval Medical Research Institute mouse (37.2 g b.w.) was perfusion-fixed with 4% paraformaldehyde and paraffin-embedded before being sectioned into 8-μm-thick slices.

One slice was placed on a 2-mm-thick barium fluoride substrate and deparafinized with a graded series of ethanol and xylene. An adjacent tissue slice was stained using haematoxylin and eosin (H&E) in order to compare hyperspectral images of the unstained tissue to those obtained with a standard microscope image (Zeiss Axio Scope.A1, Carl Zeiss Microscopy GmbH, Jena, Germany).

2.2 *Instrumentation*

2.2.1 *QCL-based infrared spectroscopy*

QCL-based measurements were obtained with a custom-built microscope. A schematic of the setup is shown in Fig. 1. The continuous-wave EC-QCL (type CW-MHF, Daylight Solutions Inc., San Diego, CA) provides a maximum output power of 50 mW and can be tuned to wavenumbers within 1030 to 1090 cm^{-1}, corresponding to wavelengths of 9.71 to 9.17 μm. The linewidth of the QCL is <1 cm^{-1}. For microspectroscopic measurements, a continuous sweep-scan over the full tuning range was performed in <12 s and repeated if necessary.

The laser beam is guided through beam shaping optics to provide homogeneous illumination of the sample and to prevent saturation of the infrared camera. Output power and wavelength of the laser can be monitored simultaneously by independently measuring the relative transmission through a thermally stabilized gas cell containing ethanol vapor and the laser power, by virtue of two uncooled pyro-electric detectors (LME353, InfraTec GmbH, Dresden, Germany). These detector signals are filtered by lock-in amplifiers (SR830, Stanford Research Systems, Sunnyvale, CA) and recorded via a general purpose interface bus.

A microbolometer FPA with 640 × 480 pixels was used for imaging. The corresponding infrared camera (VarioCAM hr head, InfraTec GmbH, Dresden, Germany) was equipped with a standard objective ($f = 50$ mm). A lens system with 12.5 mm focal length was placed in front of the camera, resulting in a nominal magnification of 4:1. The resulting projected

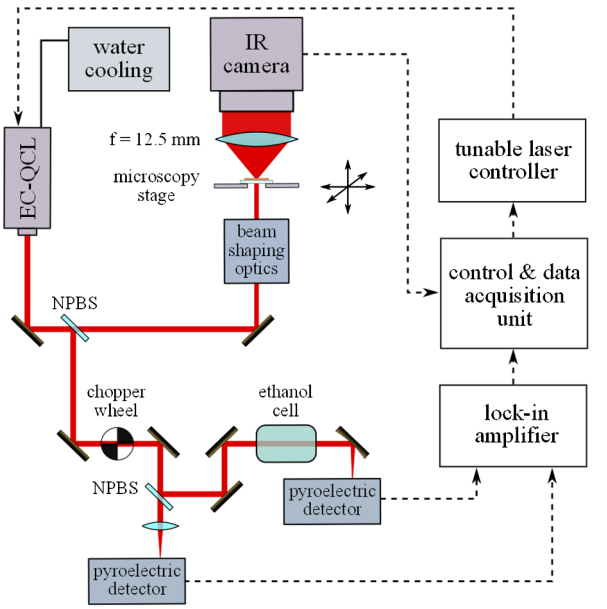

Fig. 1 Experimental setup: Infrared radiation is emitted from the external cavity quantum cascade laser (QCL). The beam is split by a nonpolarizing beam-splitter for simultaneous power- and wavelength-monitoring as well as sample illumination. NPBS, nonpolarizing beam-splitter.

pixel pitch in the sample plane was determined to be 7.3 ± 0.2 μm. The maximum field of view amounted to 3.1×2.8 mm^2. The maximum frame rate of the camera is 50 Hz. A single frame was recorded without laser illumination in order to allow for background correction. The laser illumination was switched on thereafter and typically 573 frames were recorded during the duration of one sweep-scan. As this sampling frequency corresponds to 8 frames per cm^{-1} of tuning, it is solely the laser linewidth of <1 cm^{-1} that governs the spectral resolution of the setup. However, in the experiments described here, the infrared images were averaged over 20 frames (which corresponds to a spectral interval width of 2.4 cm^{-1}) in order to allow for a better comparison with the FT-IR spectroscopy. For FT-IR experiments, a spectral resolution of 4 cm^{-1} and an interval width of 2 cm^{-1} were chosen. In passing, we would like to note that a spectral resolution of 4 cm^{-1} will frequently suffice for resolving the typical linewidth occurring in the case of biomedical samples.

A combination of a piezo-driven XY-translation stage (M686, Physik Instrumente GmbH & Co. KG, Karlsruhe, Germany) and a dc-motor driven linear actuator as Z-stage (M414.1PD, Physik Instrumente GmbH & Co. KG) were used to position the sample with a bidirectional repeatability of 0.3 μm in XY-direction and 1 μm in Z-direction.

In order to utilize the benefits of spatial oversampling, sample absorbance was repeatedly measured after translation of the sample by half of the pixel pitch in the object plane along both the x- as well as the y-directions. The resulting four images were combined into one image with an effective pixel resolution of half the original pixel pitch, i.e., ith ~3.6 μm in either direction. The optical resolution of the overall system was determined independently to be 9 μm and was, thus, diffraction limited.[22]

For reference, one absorbance measurement of this type is performed on an empty barium-fluoride substrate without spatial oversampling. In addition, environmental influences and substrate-to-substrate variations are compensated for by the

additional referencing onto empty areas of that substrate, which carries the tissue.

For each absorbance measurement, the laser was tuned over its full tuning range for five times, resulting in an acquisition time of 5 min or less.

2.2.2 *FT-IR imaging*

For comparison, FT-IR imaging was performed at the setup available at the IR beamline at the synchrotron light source Angstrom Source Karlsruhe (ANKA). Note that, however, the measurements described in this paper were performed with a globar illuminating the sample. The commercial IR microscope (Hyperion 3000, Bruker Optik GmbH, Ettlingen, Germany) was equipped with a liquid nitrogen-cooled MCT-FPA with 40 μm pixel pitch. A 15× magnification objective resulted in a projected pixel pitch of 2.7 μm in the sample plane and a total field of view of 171×171 μm^2. Detailed characterization of the setup can be found in Ref. 23.

IR spectra ranging from 1000 to 2000 cm^{-1} with 4 cm^{-1} resolution and 128 scans per measurement were acquired. The total acquisition time was 17 min per image, including both the sample and reference measurement.

2.2.3 *FT-IR mapping*

FT-IR mapping was performed with a commercial infrared microscope (Hyperion 1000, Bruker Optik GmbH) coupled to an FT-IR spectrometer (Tensor 27, Bruker Optik GmbH). A single-element liquid nitrogen-cooled MCT detector was used. The aperture was set to a diameter of 8.3 μm. The sample was mapped with a step size of 3 μm, resulting in an approximately threefold spatial oversampling. The field of view was chosen to match the experimental conditions of the FT-IR imaging experiments, such that a total of 57×57 infrared spectra were measured, which results in a total field of view of 171×171 μm^2.

IR spectra ranging from 1000 to 4000 cm^{-1} with 4 cm^{-1} resolution and 30 scans per measurement were also acquired. Acquisition time for the complete image, including reference measurements, amounted to 18 h.

2.3 *k-means clustering for color-coding of infrared spectra*

Color-coded images were derived from the hyperspectral data by use of the k-means clustering algorithm from the MATLAB® statistics toolbox (R2013a, The MathWorks Inc., Natick, MA). The procedure was unsupervised and a target number of five clusters was chosen.

The iterative process aims to minimize the mean distance from spectra to the centroid of their respective cluster. In so doing, highly similar spectra are assigned to the same cluster. Upon completion of the clustering, each absorbance spectrum is labeled as being a member of one cluster to which an arbitrary color can be assigned. The visualization of the labels in a labeled image, thus, highlights the spatial distribution of distinct spectroscopic features.

Throughout the work described in this paper, the infrared datasets were partitioned into five clusters. Color assignment was determined by the average absorbance of the centroid spectrum of the respective cluster (e.g., cyan indicates the cluster with the highest average absorbance).

3 Results

Figure 2(a) shows an H&E-stained section of mouse jejunum obtained with a conventional light microscope. Absorbance of the adjacent unstained tissue slice was measured with the QCL-based infrared microscope and k-means clustering was performed to partition the data. The clustering was performed over the spectroscopic region from 1030 to 1090 cm^{-1}. The resulting label image [Fig. 2(b)] covers a sample area of 8.7 mm^2.

A sample section with an area of 0.03 mm^2 is highlighted with a box in Fig. 2(b). Infrared absorbance spectra in this

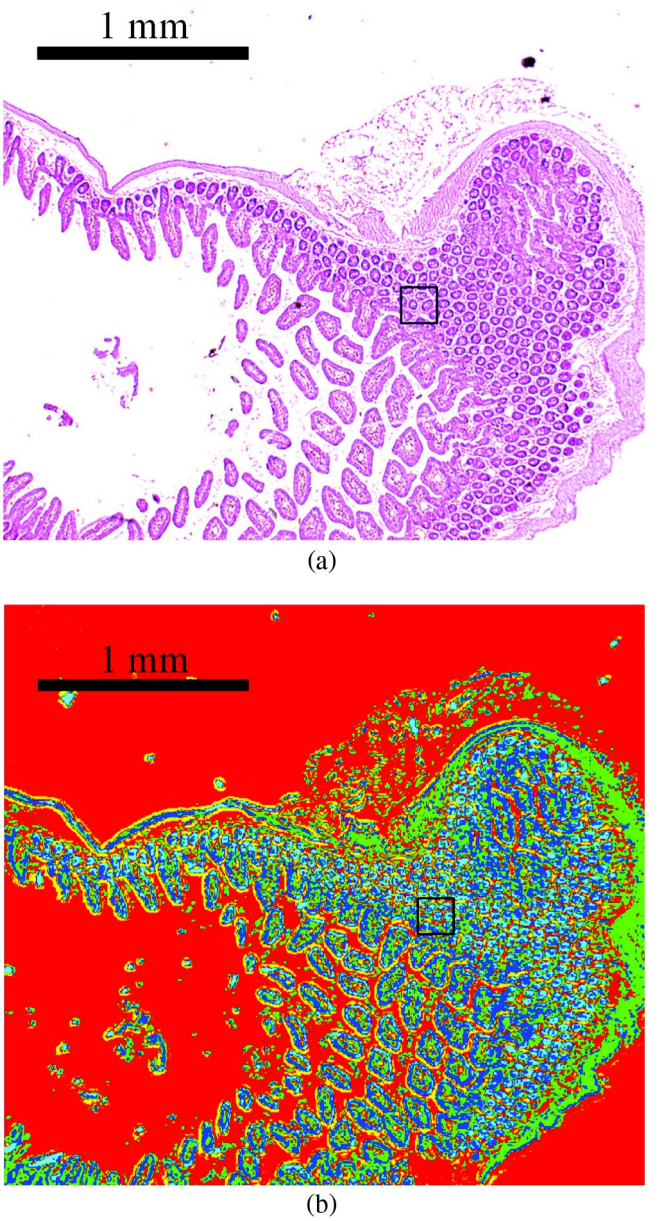

Fig. 2 (a) Image of haematoxylin and eosin-stained section of mouse jejunum. The center of the slice shows villi surrounded by crypts and smooth muscle tissue of the lamina muscularis. (b) Corresponding infrared label image of the adjacent unstained tissue slice, measured with QCL-based imaging. The total acquisition time of the complete infrared image of 3.1×2.8 mm^2, including the reference measurement, amounted to 5 min. The box indicates the area used for comparing the QCL-based imaging with other infrared methods (see Fig. 3). The clustering was performed in the spectroscopic region from 1030 to 1090 cm^{-1}.

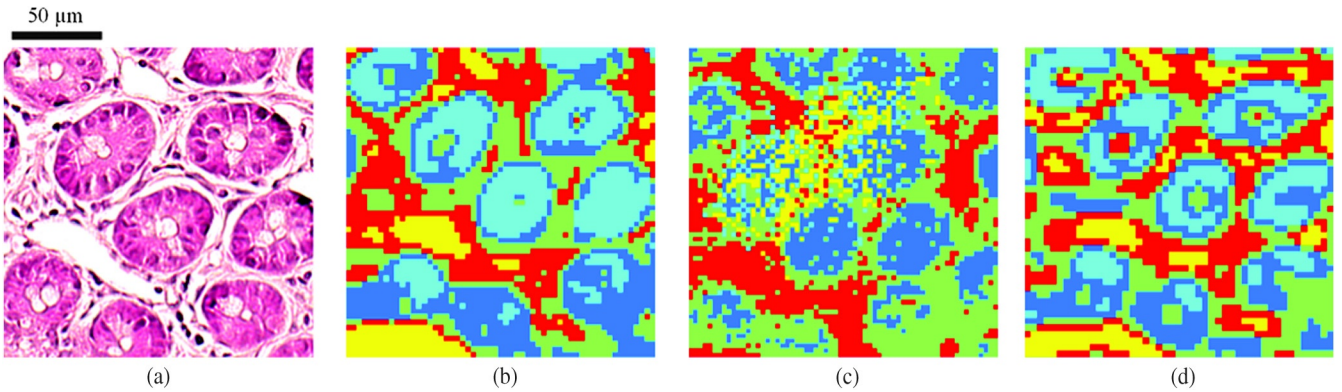

Fig. 3 (a) Extended view of the H&E-stained section of mouse jejunum representing the area marked with a box in Fig. 2(a). Several crypts can be identified. Corresponding label images of the unstained adjacent tissue slice were obtained via (b) Fourier transform infrared (FT-IR) mapping, (c) FT-IR imaging, and (d) QCL-based imaging. (Note that the field of view is slightly shifted in the FT-IR imaging measurement for technical reasons.) See text for color code. Note that clustering was performed using the full spectral range that was available to each experimental setup individually.

area were collected using FT-IR mapping as well as FT-IR imaging. FT-IR mapping and FT-IR imaging spectra were baseline corrected prior to cluster analysis of the datasets. The resulting label images are shown in Fig. 3(b) (FT-IR mapping) and Fig. 3(c) (FT-IR imaging). The corresponding QCL-based hyperspectral data were extracted from the full dataset (i.e., 8.7 mm^2). The label image shown in Fig. 3(d) resulted from cluster analysis within this subset of spectra. The full spectral range of each experiment was used for clustering. In passing we would like to note that a similar infrared image is obtained for the case of FT-IR mapping [Fig. 3(b)], if the data analysis is restricted to 1030 to 1090 cm^{-1}, i.e., the spectral range that is available to the QCL measurement.

For direct comparison of FT-IR and QCL-based spectroscopy, the spectrum averaged over the reduced sample area is shown in Fig. 4 for the two methods, FT-IR mapping (dashed line) and QCL-based imaging (solid line). For better comparison, the raw average data are presented and, in particular, no baseline correction was performed.

4 Discussion

Figure 2(b) demonstrates the large field of view of the QCL-based setup. The cyan and blue clusters indicate the epithelium. Crypts and villi, thus, can be located, with cyan being more concentrated in crypts. The green cluster is mainly attributed to smooth muscle tissue on the right side of the image (*lamina muscularis mucosae*). The green areas inside the villi could also indicate smooth muscle cells, and the green pixels between the crypts, connective tissue (*lamina propria mucosae*). Red was assigned to regions with almost no absorption. Pixels assigned to the yellow cluster are concentrated at edges of the tissue. Both red and yellow pixels were also found in connective tissue.

Figure 3 demonstrates the achievable resolution using FT-IR imaging, FT-IR mapping, and QCL-based hyperspectral imaging. FT-IR imaging [Fig. 3(c)] appears to produce the image with the least contrast. We speculate that this result is caused mainly by baseline irregularities of the specific MCT-FPA used for this measurement, which are described in more detail in Ref. 23. The images obtained with FT-IR mapping [Fig. 3(b)] and QCL-based setup [Fig. 3(d)] show similar tissue morphology. There appear to be two clusters (cyan and blue) that indicate crypt epithelium. An obvious difference in lateral

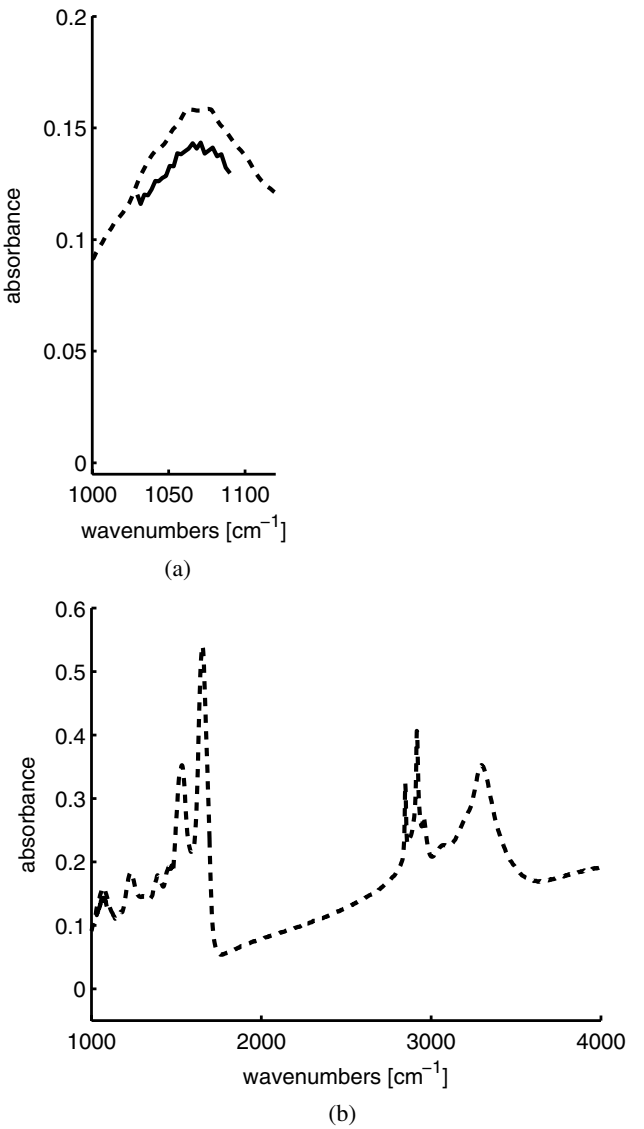

Fig. 4 Spectra averaged over the reduced sample area: FT-IR mapping (dashed line) and QCL-based imaging (solid line). For better comparison, no baseline correction was performed prior to averaging. (a) Wavenumber region from 1000 to 1120 cm^{-1} (b) Wavenumber region from 1000 to 4000 cm^{-1}.

Table 1 Comparison of the three presented techniques for hyperspectral imaging. Note that the wavenumber resolution was artificially increased from <1 to 4 cm^{-1} in the case of quantum cascade laser (QCL) imaging in order to allow for a better comparison.

	FT-IR mapping	FT-IR imaging	QCL imaging
System	Bruker Hyperion 1000	Bruker Hyperion 3000	Custom-built
Source	Globar	Globar	QCL
Detector	Single MCT	MCT-FPA 64×64	Microbolometer FPA 640×480
Liquid nitrogen cooling	Yes	Yes	No
Wavenumber range (cm^{-1})	1000 to 4000	1000 to 2000	1030 to 1090
Wavenumber resolution (cm^{-1})	4	4	4
Field of view (mm^2)	0.17×0.17	0.17×0.17	2.8×3.1
Pixel pitch / step width (μm)	3	2.7	3.6
Spatial resolution (μm)	8.3	<10	9
Total acquisition time (min)	1080	17	5
Normalized measurement time $T[s/(mm^2\,cm^{-1})]$	738.7	11.6	0.6

Note: FT-IR, Fourier transform infrared; MCT, mercury-cadmium-telluride; FPA, focal plane array.

resolution cannot be observed; however, the central lumen of the crypts appear to be sharper in Fig. 3(d). The clustering of connective tissue surrounding the crypts seems to differ slightly.

Figure 4(b) demonstrates the small spectral bandwidth of the QCL-based setup used in this experiment compared to the FT-IR mapping experiment. In order to compare the raw spectra, no baseline correction was performed. The average spectra of the reduced sample area obtained by QCL-based imaging and FT-IR mapping match reasonably well [Fig. 4(a)]. The QCL-based spectra show slightly lower absorbance values. We speculate that this is caused by the missing baseline correction. Note that the fluctuations of the QCL-based spectrum (noise) are mainly caused by the substantially shorter acquisition time (see Table 1) when compared to the case of FT-IR spectroscopy. Furthermore, only a few percent of the total laser power is used for illuminating the small clipping shown in Fig. 2(b). In turn, when evaluating larger sample sizes, the signal-to-noise ratio of the mean signal is much better than the data shown in Fig. 4(a) and signal-to-noise ratios as low as 0.004 a.u. have been achieved in the central area (25%) of the full field of view.[22]

All setups accurately discriminate between crypt epithelium and the surrounding connective tissue, which, vice versa, indicates that the spectral region from 1030 to 1090 cm^{-1} (e.g., carbohydrates, peptides) potentially bares enough information in order to obtain correct classification results for the assessment of morphology. Label images obtained with FT-IR mapping and the QCL-based measurements reveal heterogeneities among crypt epithelia. In the case of QCL-based measurements, this might hint at the distribution of highly glycosylated peptides.[24] Spectral differences in the region of 1000 to 1100 cm^{-1} have already been used to identify malignant colon tissue epithelium using FT-IR mapping with a large sample size but at low resolution.[4] Future experiments will be required to verify whether adenocarcinomas in colon tissue can be detected using the QCL-based setup.

For comparison, Table 1 shows the parameters used for the three presented techniques. To put the acquisition times into perspective, the acquisition times for the measurements presented in this paper are normalized for better comparison by defining a value T, which enumerates the total acquisition time of the measurement, including reference measurements divided by the product of field of view and width of the spectral interval.

The values of the normalized measurement time T clearly illustrate the speed advantage of the QCL-based setup. This advantage is achieved by combining the QCL source with a microbolometer FPA with high pixel count, resulting in a large field of view without any compromises in spatial resolution. If the relatively small tuning range of the QCL-based setup is sufficient, it can be used for rapid hyperspectral imaging.

Future experiments will have to clarify whether or not a limited spectral bandwidth may cause problems for practical application of QCL-based imaging in more general cases of histopathology. Methods such as extended multiplicative signal correction may allow for further improvements upon an increase in spectral bandwidth. It appears feasible to extend the experimental scheme shown here to a broad spectral range covering several hundred cm^{-1} in wavenumber by combining multiple QCLs into one setup.[22]

The broad availability, dropping costs, and increasing tuning ranges of EC-QCLs may lead to the standard use of QCL-based imaging with microbolometer FPAs in both histopathology and vibrational microspectroscopy in general.

Acknowledgments

We acknowledge the synchrotron light source ANKA for provision of instruments at their beamlines and would like to thank D. Moss and M. Süpfle for their assistance in using beamline IR2. We would also like to thank M. Arnold for the helpful discussions regarding infrared optics. J. Vogt and A. Schönhals acknowledge support by the Heidelberg Graduate School of Fundamental Physics. This work was financed by Baden-Württemberg Stiftung.

References

1. S. Argov et al., "Diagnostic potential of Fourier-transform infrared microspectroscopy and advanced computational methods in colon cancer patients," *J. Biomed. Opt.* **7**(2), 248–254 (2002).
2. M. Diem et al., "A decade of vibrational micro-spectroscopy of human cells and tissue (1994–2004)," *Analyst* **129**, 880–885 (2004).
3. P. Lasch and W. Petrich, "Data acquisition and analysis in biomedical vibrational spectroscopy," in *Biomedical Applications of Synchrotron Infrared Microspectroscopy*, D. Moss, Ed., RSC Publishing, Cambridge (2011).
4. P. Lasch et al., "Imaging of colorectal adenocarcinoma using FT-IR microspectroscopy and cluster analysis," *Biochim. Biophys. Acta* **1688**, 176–186 (2004).
5. C. Petibois and G. Déléris, "Chemical mapping of tumor progression by FT-IR imaging: towards molecular histopathology," *Trends Biotechnol.* **24**, 455–462 (2006).
6. R. Wolthuis et al., "IR spectral imaging for histopathological characterization of xenografted human colon carcinomas," *Anal. Chem.* **80**, 8461–8469 (2008).
7. A. Travo et al., "IR spectral imaging of secreted mucus: a promising new tool for the histopathological recognition of human colonic adenocarcinomas," *Histopathology* **56**, 921–931 (2010).
8. R. K. Sahu et al., "Detection of abnormal proliferation in histologically 'normal' colonic biopsies using FTIR-microspectroscopy," *Scand. J. Gastroenterol.* **39**, 557–566 (2004).
9. R. K. Sahu et al., "Prediction potential of IR-micro spectroscopy for colon cancer relapse," *Analyst* **135**, 538–544 (2010).
10. P. Dumas et al., "Imaging capabilities of synchrotron infrared microspectroscopy," *Faraday Discuss.* **126**, 289–302 (2004).
11. L. M. Miller and P. Dumas, "Chemical imaging of biological tissue with synchrotron infrared light," *Biochim. Biophys. Acta* **1758**, 846–857 (2006).
12. E. Levenson, P. Lerch, and M. C. Martin, "Infrared imaging: synchrotrons vs. arrays, resolution vs. speed," *Infrared Phys. Technol.* **49**, 45–52 (2006).
13. M. J. Nasse et al., "Synchrotron infrared microspectroscopy imaging using a multi-element detector (IRMSI-MED) for diffraction-limited chemical imaging," *Nucl. Instrum. Methods Phys. Res. A* **582**, 107–110 (2007).
14. M. J. Nasse et al., "Multi-beam synchrotron infrared chemical imaging with high spatial resolution: beamline realization and first reports on image restoration," *Nucl. Instrum. Methods Phys. Res. A* **649**, 172–176 (2011).
15. D. L. Wetzel and M. J. Nasse, "Synchrotron infrared confocal microspectroscopic spatial resolution or a customized synchrotron/focal plane array system enhances chemical imaging of biological tissue or cells," *Nucl. Instrum. Methods Phys. Res. A* **649**, 179–183 (2011).
16. J. Faist et al., "Quantum cascade laser," *Science* **264**, 553–556 (1994).
17. F. Capasso, "High-performance midinfrared quantum cascade lasers," *Opt. Eng.* **49**, 11102 (2010).
18. F. Niklaus, C. Vieider, and H. Jakobsen, "MEMS-based uncooled infrared bolometer arrays—a review," *Proc. SPIE* **6836**, 68360D (2007).
19. M. C. Phillips and N. Hô, "Infrared hyperspectral imaging using a broadly tunable external cavity quantum cascade laser and microbolometer focal plane array," *Opt. Express* **16**, 1836–1845 (2008).
20. M. R. Kole et al., "Discrete frequency infrared microspectroscopy and imaging with a tunable quantum cascade laser," *Anal. Chem.* **84**, 10366–10372 (2012).
21. M. C. Phillips and B. E. Bernacki, "Hyperspectral microscopy of explosives particles using an external cavity quantum cascade laser," *Opt. Eng.* **52**(6), 061302 (2013).
22. N. Kröger et al., "Rapid hyperspectral imaging in the mid-infrared," *Proc. SPIE* **8939**, 89390Z (2014).
23. D. Moss, B. Gasharova, and Y.-L. Mathis, "Practical tests of a focal plane array detector microscope at the ANKA-IR beamline," *Infrared Phys. Technol.* **49**, 53–56 (2006).
24. C. Krafft, "Vibrational spectroscopic imaging of soft tissue," in *Infrared and Raman Spectroscopic Imaging*, R. Salzer and H. W. Siesler, Eds., Wiley-VCH, Weinheim (2009).

Biographies of the authors are not available.